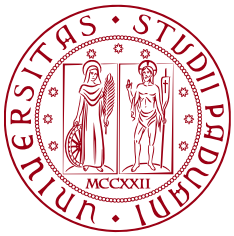

Università degli Studi di Padova
Dipartimento di Fisica e Astronomia 'Galileo Galilei'

Corso di Laurea Magistrale in Astronomia

Tesi di Laurea Magistrale

Non-equilibrium Bayesian modelling of the Sagittarius dwarf galaxy and its tidal stream

Laureando

Raphaël Errani

Relatori

Jorge Peñarrubia
Institute for Astronomy
University of Edinburgh

Giuseppe Tormen
Dipartimento di Fisica e Astronomia 'Galileo Galilei'
Università degli Studi di Padova

Padova, 9 Ottobre 2015

Abstract

Recent studies have shown that the distribution of Dark Matter within dwarf spheroidal galaxies can be constrained by measuring simultaneously dynamical properties of the remnant progenitor and its stellar tidal stream. We apply this method to determine the distribution of Dark Matter within the Sagittarius dwarf galaxy. Because of the current position of the Sagittarius dwarf along its orbit in proximity to pericentre, it is perturbed by tidal forces and not in dynamical equilibrium. We build a catalogue of high-resolution, non-equilibrium N-body models for the Sagittarius dwarf galaxy and construct a Bayesian framework to directly compare the models to observational data.

Contents

1 Introduction

Dwarf spheroidal (dSph) galaxies, situated at the faint end of the galaxy luminosity function, reveille fundamental properties of Dark Matter (DM): their density profile and the emission of γ-rays puts strong constraints on possible DM particle masses and cross sections (e.g. Macciò et al., 2012; Rocha et al., 2013; Lovell et al., 2014; Vogelsberger et al., 2014). The density profile is also sensitive to possible interactions between baryons and DM and therefore sets the foundations for understanding galaxy formation on small scales (e.g. Navarro et al., 1996; Peñarrubia et al., 2012; Di Cintio et al., 2014; Pontzen & Governato, 2014; Nipoti & Binney, 2015).

Measuring the distribution of DM in dSph galaxies is non-trivial because of the small number of observable tracers of the gravitational potential, and the degeneracy between mass and the anisotropy of the velocity dispersion which arises when working with projected quantities only. Studies of the same datasets, conducted using differing methods, remain inconclusive, indicate the existence of either constant-density cores, $d\ln\varrho/d\ln r \to 0$ for $r \to 0$, or diverging central density cusps, $d\ln\varrho/d\ln r \to \text{const}$ (e.g. Walker & Peñarrubia, 2011; Amorisco & Evans, 2012; Breddels & Helmi, 2013; Richardson & Fairbairn, 2014; Strigari et al., 2014).

In a recent study (Errani, Peñarrubia & Tormen, 2015, hereafter EPT15), we have shown that the distribution of DM in dSph galaxies leaves footprints in the morphology and dynamics of the stellar streams which form during tidal interaction with a larger galaxy. By measuring morphological and kinematic properties of both a remnant progenitor as well as its stellar stream, strong constraints on the distribution of DM in the dSph galaxy can be set.

Here we build a framework to apply this method to existing kinematic data of the Sagittarius (Sgr) dwarf galaxy. This dwarf galaxy orbits the Milky Way on an almost polar orbit and is currently at a distance of 28 kpc to the Solar System (Ibata et al., 1997; Siegel et al., 2007). Both leading and a trailing tails of tidal debris have been discovered and wrap around the Milky Way for more than one orbital period (Majewski et al., 2003; Belokurov et al., 2014).

The Sgr dwarf galaxy has just passed pericentre is therefore highly perturbed by tidal forces. We construct a catalogue of non-equilibrium N-body models to later compare them directly to observational data. In this section, we briefly review our method for constraining the distribution of DM in dSph galaxies using observational data of a remnant progenitor and its tidal stream. In section 2 we describe our numerical set-up to generate the catalogue of non-equilibrium models. We introduce the statistical framework for the Bayesian analysis in section 3. In section 4 we present preliminary results of the N-body catalogue and discuss selected models. We review our results and give an outlook for future work in section 5.

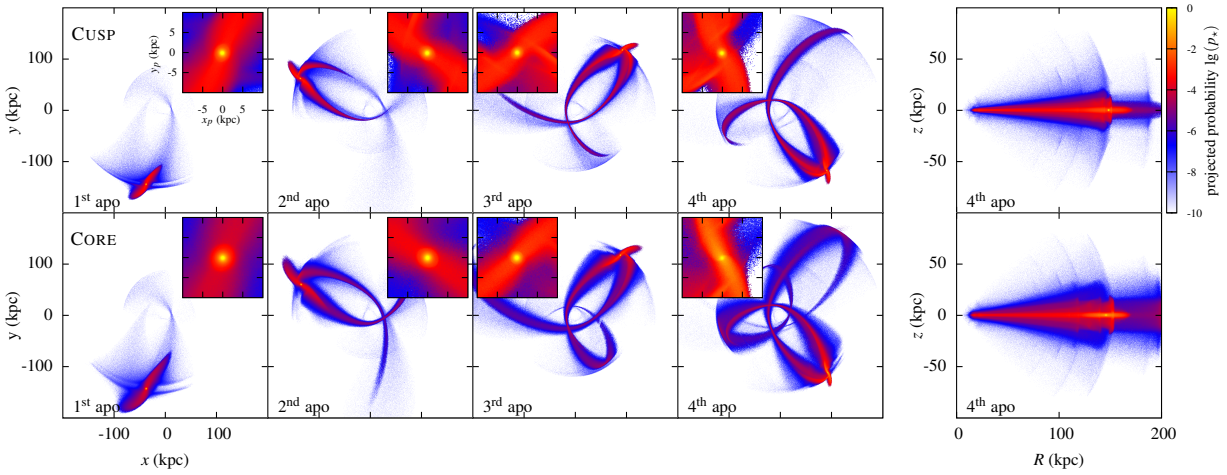

Figure 1: Snapshots of the evolution of tidal streams associated to cuspy (top row) and cored (bottom row) models (from EPT15). Small boxes in each panel show a detail view of the progenitor. The rightmost column shows the projection of tidal stream and progenitor on the (R, z) plane, where R is the cylindrical distance from the galactic centre and z is the distance above the orbital plane of the progenitor. DM particles are colour-coded according to their probability $p_\star$ of tagging stars.

1.1 Tidal evolutionary tracks for dSph galaxies

In EPT15, we study the different evolution of dSph galaxies embedded in cuspy and cored DM haloes undergoing tidal stripping in the halo of a larger galaxy using N-body simulations.

The DM of the dSph progenitors is modelled by 2×10^7 particles drawn from a Dehnen (1993) distribution function. Under the assumption that stars behave as massless and collisionless tracers of the underlying DM potential, we follow the approach by Bullock & Johnston (2005), where each DM particle is assigned a probability of representing a star in such a way that the overall stellar density profile follows a Plummer sphere with segregation $r_\star/a \simeq r_h/(1.3a)$, where r_h and $r_\star$ are the half-light and core radii of the Plummer model.

For easier comparison between cored and cuspy models, the dSph parameters are chosen such that for a given segregation $r_\star/a$, both cored and cuspy DM profiles have the same mass enclosed within the half-light radius $m_h \equiv m(< r_h)$ at $t = 0$. For the simulation itself we use the particle-mesh code SUPERBOX (see Fellhauer et al., 2000). This code samples the density on to three grids with different resolution and performs a leapfrog integration to solve the equations of motion (the code will be discussed with more detail in section 2). For these models each grid consists of 128 cells per dimension. Grid 1 resolves the core of the progenitor with a resolution of $2a/126 \approx 16$ pc, while grids 2 and 3 have resolutions of $20a/126 \approx 160$ pc and $400a/126 \approx 3.2$ kpc, respectively. We use a fixed time step of 1 Myr.

Figure 1 shows two N-body models with 2×10^7 particles which at $t = 0$ have equal observable properties, i.e. equal half-light radius r_h and average velocity dispersion σ_h within the half-light

radius. The cored model loses stars at a faster temporal pace than its cuspy counterpart, and their tidal streams differ in width.

We studied the evolution of the dSph progenitor galaxy separately from the evolution of the stream. Normalizing observable quantities like the half-light radius r_h and average velocity dispersion σ_h by their initial values $r_{h,0}$ and $\sigma_{h,0}$, and plotting these values in function of the normalized remnant progenitor mass enclosed within the half-light radius $m_h/m_{h,0}$, we find the *tidal evolutionary tracks* shown in figure 2: independently of the progenitor orbit or the absolute values of the initial progenitor properties, dSphs undergoing tidal stripping evolve along well-defined tracks which are function of the remnant progenitor mass. These tracks have a different functional form depending on the underlying DM profile: the half-light radii of cuspy galaxies stay almost constant during tidal stripping, while cored dSphs expand; cored dSphs cool down more effectively and lose stars less easily than their cuspy counterparts. The tidal tracks also depend on how deeply embedded the stellar profile is within the dSph DM halo, i.e. on the segregation parameter $r_\star/a$.

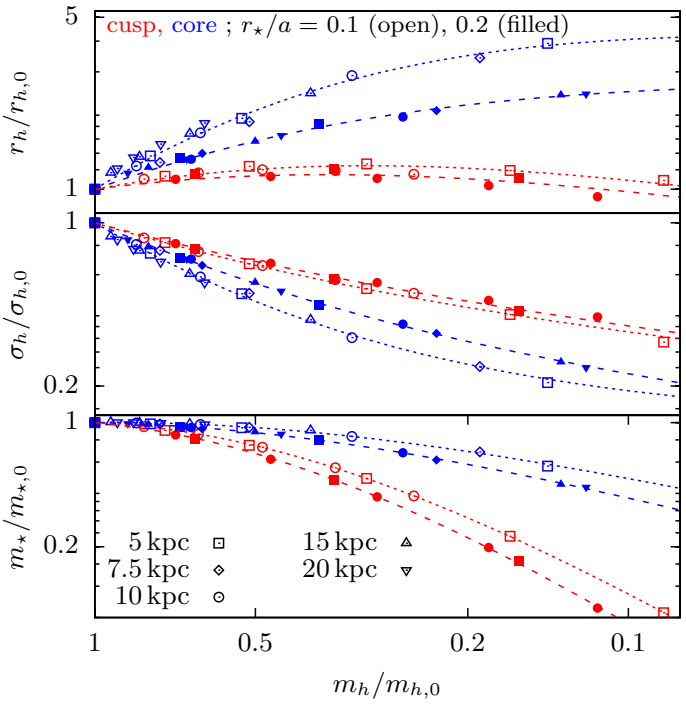

Figure 2: Evolutionary tracks for cuspy and cored dSph galaxies (from EPT15). The half-light radius r_h, the luminosity average velocity dispersion σ_h within r_h and the total stellar mass $m_\star$ are normalised to the initial value and are plotted as a function of the mass $m_h/m_{h,0}$ enclosed within r_h.

We parametrize the evolutionary tracks using the empirical formula of Peñarrubia et al. (2008)

$$f(x) = \frac{2^\alpha x^\beta}{(1+x)^\alpha} \quad \text{where} \quad x = m_h/m_{h,0} \quad . \tag{1}$$

The best-fitting parameters are listed in table 1 and the resulting tracks are plotted with dashed lines in figure 2.

Table 1: Empirical fit parameters to the tidal evolutionary tracks (from EPT15).

	$r_\star/a$		$r_h/r_{h,0}$	$\sigma_h/\sigma_{h,0}$	$m_\star/m_{\star,0}$
Cusp	0.1	α	1.49	-0.88	3.43
		β	0.35	0.24	1.86
	0.2	α	1.22	-0.68	3.57
		β	0.33	0.26	2.06
Core	0.1	α	2.91	-2.56	1.43
		β	0.15	0.05	0.69
	0.2	α	1.63	-1.39	0.82
		β	0.03	0.29	0.82

1.2 Constraints on the distribution of DM in dSphs from tidal streams

We now normalise width and velocity dispersion of the tidal stream by the corresponding properties of the dSph progenitor. Figure 3 shows the normalised width $\tilde{w}$ in function of the normalised velocity dispersion $\tilde{\sigma}$ for a fixed snapshot taken at the 4$^{\text{th}}$ apocentre of the simulation shown in figure 1. Particles which became unbound during the same pericentre passage form a *wrap*. Within a wrap, the stream width increases with galactocentric distance, while the stream velocity dispersion decreases. This can be interpreted as a consequence of Liouville's theorem stating the conservation of phase-space volume. Wraps from earlier pericentre passages are dynamically hotter, and more recent wraps show more noise as particles had less time to spread around an entire orbit. Interestingly, there is a constant offset in velocity dispersion between corresponding wraps of cuspy and cored models: tidal streams of cored progenitors are hotter and narrower than their cuspy counterparts.

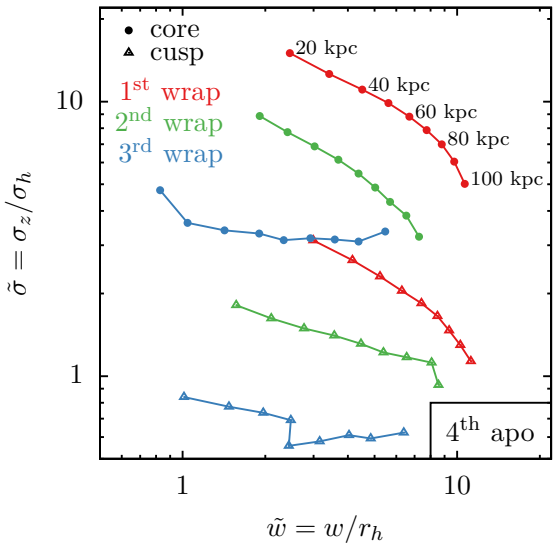

Figure 3: Width $\tilde{w}$ and velocity dispersion $\tilde{\sigma}$ of the streams normalized to the half-light radius and luminosity-averaged velocity dispersion of the progenitor dSph, respectively (from EPT15). We show data at a fixed snapshot (4$^{\text{th}}$ apocentre). Symbols are colour-coded according to the pericentric passage at which particles became unbound.

To understand the time-dependence of the above observations, we now compare the ratios of the relative width $\tilde{w}$ and velocity dispersion $\tilde{\sigma}$ for cuspy and cored galaxies for different snapshots. As the offset between wraps at a fixed snapshot is constant, all data points $(\tilde{w}, \tilde{\sigma})$ belonging to the same snapshot collapse to a rather small region in figure 4.

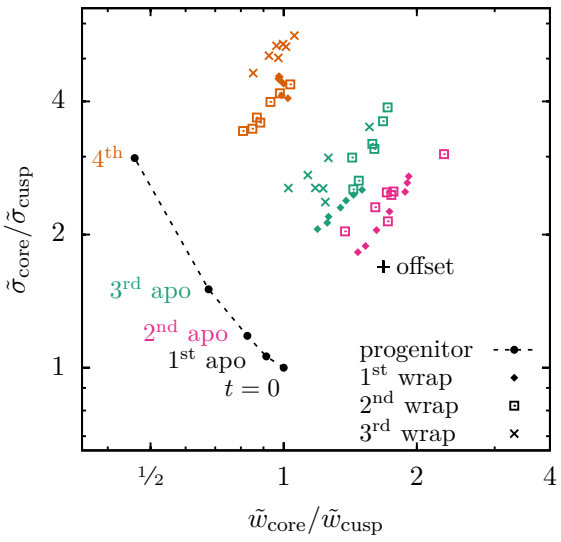

Figure 4: Time evolution of the width and velocity dispersion ratios between streams associated to dSphs embedded in cored and cuspy dark matter haloes (from EPT15). Symbols denote particles lost at different pericentric passages, whereas colours distinguish between different snapshots. The tidal evolutionary tracks are plotted with a dotted line for ease of reference.

We observe that the offset in velocity dispersion between cuspy and cored models increases with time. Plotting as a reference the tidal evolutionary tracks, we see that the time evolution of $(\tilde{w}, \tilde{\sigma})$ is mainly driven by the disparate evolution of the progenitors. As cored progenitors cool down more efficiently than cuspy ones, their tidal streams seem relatively hotter, and as cored progenitors have increasing half-light radii during tidal stripping, their tidal streams seem narrower. The intrinsic offset, marked with a black cross in figure 4, can be estimated analytically by assuming that the stream width is proportional to the tidal radius of the progenitor at pericentre $r_t \propto M^{1/3}$ (see e.g. Amorisco, 2015) and that the velocity dispersion of the stream scales as $\sigma_z \propto \sqrt{m(<r_t)/r_t}$.

For models in equilibrium, the progenitor properties follow the tidal evolutionary tracks, and models that reproduce the observed r_h and σ_h lead to $M_{\rm core} > M_{\rm cusp}$. Having set the initial conditions for the dSph, the next step corresponds to modelling the tidal stripping of the progenitor. Our results suggest that the velocity dispersion of stellar streams of cuspy models lie systematically below that of the cored models, which in turn can be used to constrain the mass profile of the progenitor by comparing the velocity dispersion of the stream against that of the remnant progenitor. In the case of the Sgr dSph, which is perturbed by tidal forces due to its vicinity to pericentre, we can't rely on the equilibrium evolution following the tidal tracks. We will therefore now develop a catalogue of non-equilibrium N-body models of the Sgr galaxy.

2 N-body models and numerical setup

2.1 Particle-mesh code

We use the particle-mesh code SUPERBOX (Fellhauer et al., 2000). This code employs a Nearest Grid Point (NGP) scheme to sample the mass density ϱ on a three-dimensional grid with $n = 2^m$ cells per dimension. For this discrete mass distribution, the solution to Poisson's equation

$$\nabla^2 \Phi_{\vec{i}} = 4\pi G \varrho_{\vec{i}} \tag{2}$$

for the cell $\vec{i}$ reads

$$\Phi_{\vec{i}} = G \sum_{\vec{j}} \varrho_{\vec{i}} H_{\vec{j}-\vec{i}}, \tag{3}$$

where Green's function

$$H_{\vec{k},\vec{k}\neq\vec{0}} = |\vec{k}|^{-1} \tag{4}$$

is a measure for the distance between two cells. $H_{\vec{0}}$ determines the interaction of particles within the same cell. For small particle numbers this value must be carefully chosen to prevent artefacts due to non-physical auto-interactions. To avoid summing over all cells in the computation of $\Phi_{\vec{i}}$, both $\varrho_{\vec{j}}$ and $H_{\vec{j}}$ are Fourier-transformed, their product is computed cell by cell in Fourier space, and the result is back-transformed to get

$$\Phi_{\vec{i}} = \frac{G}{n^3} \sum_{\vec{j}} \hat{\varrho}_{\vec{j}} \hat{H}_{\vec{j}} \exp\left(\frac{2\pi i}{n} \vec{i} \cdot \vec{j}\right) \ . \tag{5}$$

A discrete Fast Fourier Transform (FFT) algorithm is used for the transformations involved in the calculation.

Usually, when using a NGP scheme, particle accelerations are computed using only the linear part $\frac{\partial \Phi}{\partial x}\big|_i$. of the slope of the gravitational potential as measured in the cell centre. SUPERBOX makes a second order approximation of the slope in function of the particle position within a cell, which in one dimension reads,

$$a = \left.\frac{\partial \Phi}{\partial x}\right|_i (x + dx) \approx \left.\frac{\partial \Phi}{\partial x}\right|_i (x) + \left.\frac{\partial^2 \Phi}{\partial x^2}\right|_i (x)\, dx \approx \frac{\Phi_{i+1} - \Phi_{i-1}}{2\Delta x} + \frac{\Phi_{i+1} + \Phi_{i-1} - 2\Phi_i}{(\Delta x)^2} dx \tag{6}$$

taking thereby into account the deviation of a particle's position from the cell's centre.

A leapfrog scheme

$$x(t+1) = x(t) + v(t)\Delta t + \frac{a(t)}{2}(\Delta t)^2 \tag{7}$$

$$v(t+1) = v(t) + \frac{a(t) + a(t+1)}{2}\Delta t \tag{8}$$

is then used to integrate the particles' equation of motion $\{\dot{x} = v,\ \dot{v} = a\}$.

Cubic grids with three different resolutions are employed to sample the density. Each grid uses the same number of cells, $n = 2^m$ per dimension, with different width r_1, r_2, r_3. The two highest resolutions grids are centred on centre of density the dwarf galaxy, which is defined by constructing a sphere of neighbouring particles within the grid of highest resolution, and re-centring the sphere iteratively on its centre of mass until convergence. The largest grid instead has a fixed position. Having different resolution grids makes it possible to account for the large difference in particle densities between the central regions of the dwarf and the tidal stream.

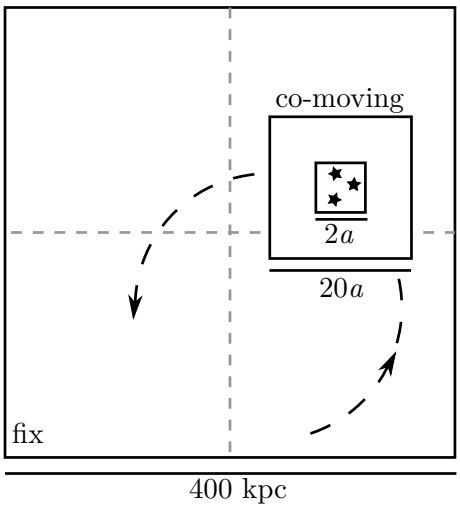

Figure 5: The particle-mesh code SUPERBOX uses three different grids to sample the density. While the outermost grid is fixed in space, the two higher-resolving grids are centred on and moving with the dwarf galaxy. We adopt $r_1 = 400\,\mathrm{kpc}$, $r_2 = 20a$ and $r_3 = 2a$, where by a we denote the scale radius of the Dehnen profile used to model the initial distribution of DM in the dSph galaxies.

2.2 Modelling of the host galaxy

We model the milky-way like host galaxy by an analytical, non-evolving potential, consisting of a spherical Bulge (Hernquist, 1990)

$$\varrho_b(r) = \frac{M_b}{2\pi}\frac{1}{r}\frac{1}{(r+a_b)^3}\ , \qquad \Phi_b(r) = -\frac{GM_b}{r+a_b}\ , \tag{9}$$

with scale radius $a_b = 1.2\,\mathrm{kpc}$ and mass $M_b = 1.3\times10^{10}\,\mathrm{M}_\odot$, an axis-symmetric disk (Miyamoto & Nagai, 1975),

$$\begin{aligned}\varrho_d(R,z) &= \frac{b_d^2 M_d}{4\pi}\ \frac{a_d R^2 + \left(a_d + 3\sqrt{z^2+b_d^2}\right)\left(a_d+\sqrt{z^2+b_d^2}\right)^2}{\left[R^2+\left(a_d+\sqrt{z^2+b_d^2}\right)^2\right]^{5/2}\left(z^2+b_d^2\right)^{3/2}} \\ \Phi_d(R,z) &= -GM\ \left[R^2+\left(a_d+\sqrt{b_d^2+z^2}\right)^2\right]^{-1/2}\ ,\end{aligned} \tag{10}$$

with radial and vertical scale lengths $a_d = 3.5\,\mathrm{kpc}$, $b_d = 0.3\,\mathrm{kpc}$ and mass $M_d = 7.5\times10^{10}\,\mathrm{M}_\odot$, and a spherical Navarro et al. (1997) (NFW) halo,

$$\begin{aligned}\varrho_h(r) &= \frac{\delta_c\varrho_c}{(r/r_h)(1+r/r_h)^2}\ , \qquad \delta_c = \frac{200}{3}\frac{c^3}{[\ln(1+c)-c/(1+c)]} \\ \Phi_h(r) &= -\frac{4\pi G\varrho_c\delta_c r_h^3}{r}\ln\left(1+\frac{r}{r_h}\right)\ ,\end{aligned} \tag{11}$$

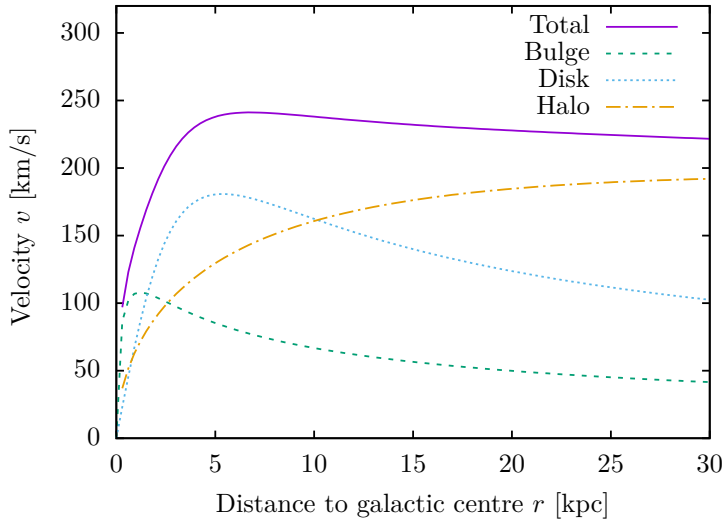

Figure 6: Rotation curve for orbits within the $z = 0$ plane.

with virial[1] radius $r_{200} = cr_h = 226\,\mathrm{kpc}$, mass $M_{200} = 1.25 \times 10^{12}\,\mathrm{M}_\odot$, concentration $c = 12$, setting $\rho_c = 3H_0^2/8\pi G$ with $H_0 = 68\,\mathrm{km/s/Mpc}$. This leads to a velocity of the local standard of rest (LSR) around the galactic centre of $v_{\mathrm{LSR}} = 240\,\mathrm{km/s}$ at $r_{\mathrm{LSR}} = -8.3\,\mathrm{kpc}$. Figure 6 shows the rotation curve for orbits within the $z = 0$ plane.

2.3 Modelling of the dwarf galaxy

The initial (Dark Matter) particle distribution for the dwarf galaxy is drawn from a Dehnen (1993) profile:

$$\varrho_{\mathrm{DM}}(r) = \frac{(3-\gamma)M}{4\pi} \frac{a}{r^\gamma (r+a)^{4-\gamma}} \,, \tag{12}$$

where $0 \leq \gamma \leq 3$ is a dimensionless parameter determining the central slope of the density profile. Figure 7 shows the density distribution for a cored ($\gamma = 0$) and a cuspy ($\gamma = 1$) profile for $a = M = 1$.

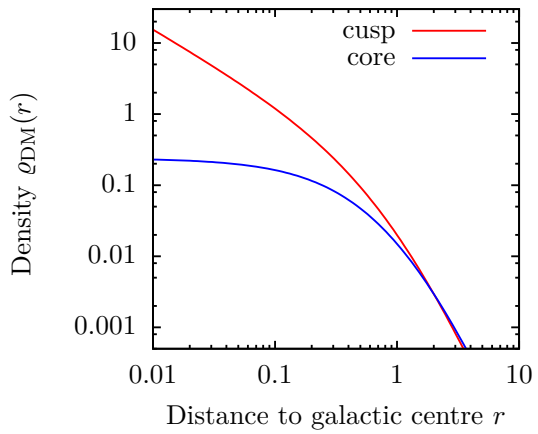

Figure 7: Density for a cored ($\gamma = 0$) and a cuspy ($\gamma = 1$) Dehnen profile with $a = M = 1$.

[1] Following Navarro et al. (1997), we define the virial radius r_{200} with the condition that the average density within is 200× larger than the critical density for closure.

Observations show that the distribution of stars within dSph galaxies is a cored distribution. We model the initial stellar distribution by a Plummer density profile,

$$\varrho_\star(r) = \varrho_0 \left(1 + \frac{r^2}{r_\star^2}\right)^{-5/2} . \tag{13}$$

This sample of stars is embedded in the potential Φ of the dwarf galaxy, and for the isotropic case the stellar velocity dispersion reads for zero systemic velocity $\langle v \rangle$:

$$\langle v^2(r) \rangle = \sigma_{v,\star}^2(r) = \frac{1}{\nu} \int_r^\infty dr\ \nu \frac{d\Phi}{dr}. \tag{14}$$

The above relation follows directly from the Jeans equation, denoting by $\nu = \varrho_\star(r)/m_\star$ the stellar number density (see Binney & Tremaine, 2008, chap. 4.8.1). For the Dehnen potentials with $\gamma = 0$ and $\gamma = 1$ there is an analytical (though long and thus omitted) expression for the integral that appears in the above equation. Following the approach of Bullock & Johnston (2005), we assign to each particle of the Dehnen DM profile a static probability p that the particle belongs to a stellar distribution function satisfying (13) and (14). As both stars and DM are collisionless components of the dwarf galaxy, this probability can be obtained immediately from the phase-space distribution functions for Dark Matter $f_{\rm DM}(\boldsymbol{r}, \boldsymbol{v})$ and stars $f_\star(\boldsymbol{r}, \boldsymbol{v})$. From Jean's theorem it is known that all distribution functions f satisfying the collisionless Boltzman equation depend on the phase-space coordinates through the energy integral only, i.e. $f = f(E(\boldsymbol{r}, \boldsymbol{v}))$. Then

$$p(E) = \frac{f_\star(E)}{f_{\rm DM}(E)} . \tag{15}$$

Marginalizing over all velocities, we see that the mass-to-light ratio

$$\phi(r) = \frac{\int f_{\rm DM}(E) d\boldsymbol{v}}{\int f_\star(E) d\boldsymbol{v}} = \frac{\varrho_{\rm DM}(r)}{\varrho_\star(r)} \tag{16}$$

must increase for cuspy dSphs for small r/a as shown in figure 8, which is intuitively explained noting that we embed a cored (constant central density) stellar profile inside a cuspy (diverging central density) DM profile.

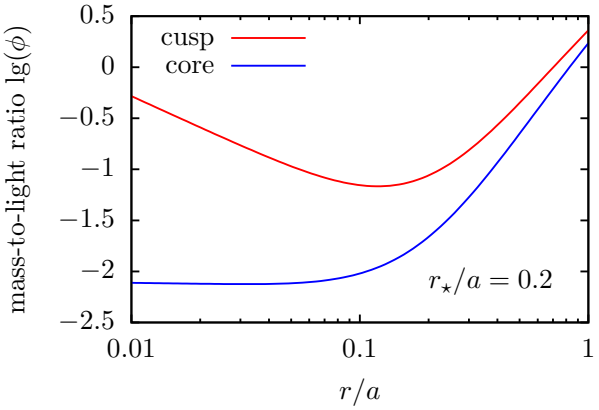

Figure 8: Mass-to-light ratio ϕ for dSphs with cored and cuspy Dehnen DM profile with scale radius a and a stellar Plummer profile with segregation $r_\star/a = 0.2$.

2.4 Initial conditions

We use cosmologically motivated initial conditions for the Sgr models. Regarding physical properties of the Sgr galaxy, this means deciding on appropriate values of the initial scale radius a for the DM Dehnen profile, as well as on the initial total mass. Let's briefly recall that for a NFW halo, the slope at scale radius r_h equals

$$\frac{\partial \ln \varrho_{\rm NFW}}{\partial \ln r}(r_h) = -2 \ .$$

For a Dehnen profile, differentiating equation (12),

$$\frac{\partial \ln \varrho_{\rm DM}}{\partial \ln r} = (\gamma - 4)\frac{r}{r+a} - \gamma \ .$$

For $\gamma = 0$, $\partial \ln \varrho_{\rm DM}/\partial \ln r = -2$ for $r = a$, while for $\gamma = 1$ we find $r = a/2$. If we now set

$$M_{200} = \underbrace{4\pi \varrho_c \delta_c r_h^3 \left[\ln(1+c) - \frac{c}{c+1}\right]}_{\rm NFW} \quad = \quad \underbrace{M_{\rm tot}\left(\frac{r_{200}}{r_{200}+a}\right)^{3-\gamma}}_{\rm Dehnen} , \tag{17}$$

then

$$\frac{M_{200}}{M_{tot}} = \left(\frac{c}{c+a/r_h}\right)^{3-\gamma} \gtrapprox \frac{1}{2} \ \text{ for } \ 0 \le \gamma \le 1, \ 1 \le a/r_h \le 2 \ , c \ge 5 \ . \tag{18}$$

The above set of equations allows us to approximately map properties of NFW haloes to our Dehnen profiles. Using the estimate of the total luminosity $L_{\rm Sgr} \approx 10^8 L_\odot$ of the Sgr dwarf of Niederste-Ostholt et al. (2010), the relation between stellar mass and DM halo mass of Moster et al. (2013) as well as the relation between the concentration parameter c and the Virial mass of Ludlow et al. (2014), we set generous limits on our parameter space for the initial physical properties of the Sgr dwarf:

$$\begin{aligned} \text{total initial mass:} \quad & 10^{10}\,{\rm M}_\odot \ \le \ M_{\rm Sgr} \ \le \ 1.5\times 10^{11}\,{\rm M}_\odot \ , \\ \text{initial DM scale radius:} \quad & 2\,{\rm kpc} \ \le \ a_{\rm Sgr} \ \le \ 16\,{\rm kpc} \ . \end{aligned}$$

The current position of the Sgr dwarf, as well as its radial velocity component, are fairly well known (see table 2).

Table 2: Galactic coordinates, distance and heliocentric radial velocity of the Sgr dwarf

l, b	$5.57°, -14.17°$	Majewski et al. (2003)
d	28.4 kpc	Siegel et al. (2007)
v_r	141 km/s	Ibata et al. (1997)

The measurements of proper motions currently available for the Sgr dwarf are too imprecise to allow for a reasonable determination of the orbit and are rather inconsistent with each other (compare e.g. Dinescu et al., 2005; Pryor et al., 2010; Massari et al., 2013). We do therefore not

use proper motion measurements to determine the orbit, but choose the current Sgr velocity vector to lie in the plane of recent tidal debris as fitted by Majewski et al. (2003):

$$\text{pole of } \textit{current} \text{ orbital plane:} \quad L, B = 87^\circ, -14^\circ \ .$$

The remaining degree of freedom in velocity space can be expressed as the distance of the most recent apocentre of the Sgr orbit. Following the detections of the Sgr tidal stream as in Belokurov et al. (2014), we choose the most recent apocentre of Sgr to lie between the recent apocentres of its leading and trailing tidal debris,

$$\text{distance of most recent apocentre to galactic centre:} \quad 60\,\mathrm{kpc} \ \leq \ R \ \leq \ 90\,\mathrm{kpc} \ .$$

Having defined the current position in phase space, we integrate a point-mass orbit backwards in time for 3 orbital periods to generate initial conditions to the N-body runs. The tidal mass-loss causes a re-distribution of orbital energy to the leading and trailing streams. The Sgr orbit thereby decays. We iteratively compensate for the orbital decay, using a multidimensional secant method for energy E, angular momentum $\boldsymbol{L}$ and orbital phase ϕ. Denoting by superscript-i initial and superscript-f final values, the iterative procedure for E reads

$$E_n = E_{\rm Sgr} + E^i_{n-1} - E^f_{n-1} \frac{E^i_{n-1} - E^i_{n-2}}{E^f_{n-1} - E^f_{n-2}} \ . \tag{19}$$

For stability, we check if the slope $(E^i_{n-1} - E^i_{n-2})/(E^f_{n-1} - E^f_{n-2})$ is physically reasonable and under-relax when necessary.

The time step $\Delta t = \min(1\,\mathrm{Myr}, t_{\rm dyn}(r_{1/2})/400)$, fixed throughout each simulation, is chosen in function of the dynamical time $t_{\rm dyn}(r) = 2\pi r^{3/2}\,(GM_r)^{-1/2}$ at half-mass radius $r_{1/2}$ of the Sgr model. The maximum time step of 1 Myr ensures that the tidal interaction with the host halo is captured with sufficient temporal resolution.

We then walk diagonally through parameter space as shown in figure 9. If a model with mass $M^\dagger$ and scale radius $a^\dagger$ disrupts before reaching the currently observed position of Sgr, all models with $(M \leq M^\dagger) \wedge (a \geq a^\dagger)$ are presumed to disrupt as well and are therefore not simulated.

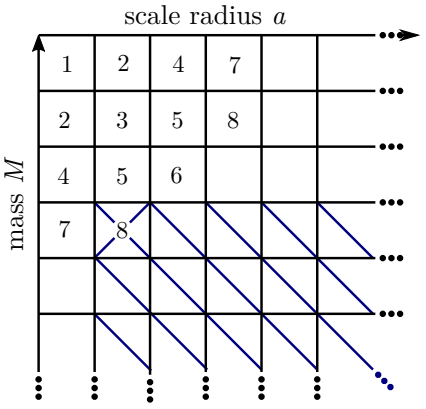

Figure 9: The simulations start with the densest model and then walk diagonally through parameter space. The numbers in the diagram indicate the priority for the order in which simulations are started. If a model with $(M^\dagger,a^\dagger)$ disrupts, models with $(M \leq M^\dagger) \wedge (a \geq a^\dagger)$ are excluded from being started.

3 Bayesian framework

3.1 Statistical model

The observational dataset we compare our N-body models to is a complete sample of M-type giants in the Sgr galaxy. For each star, we have a position on the sky α_d, δ_d and a radial velocity measurement v_d. From the average distance to its neighbouring stars we can define a surface brightness Σ_d for each position.

$$\text{Observational data :} \qquad d \equiv \{(v_d, \Sigma_d)_1, (v_d, \Sigma_d)_2, ..., (v_d, \Sigma_d)_N\}$$

The parameters of our N-body models are the central slope of the density profile γ, apocentre distance R, dark matter scale radius a, stellar scale radius $r_\star$ and total mass M.

$$\text{Model parameters :} \qquad \theta_\alpha \equiv (\gamma_{\alpha_1}, R_{\alpha_2}, a_{\alpha_3}, r_{\star\alpha_4}, M_{\alpha_5})$$

What's the probability $P(\theta_\alpha|d)$ of a set of model parameters θ_α given the observational data d? Most importantly: how tight are our constraints on γ? In other words, we are interested in determining

$$P(\theta_\alpha|d) = \frac{P(d|\theta_\alpha)P(\theta_\alpha)}{P(d)} \quad \text{(Bayes)}. \tag{20}$$

To do so, we first need to define a way to compute the likelihood $P(d|\theta_\alpha)$. The N-body models consists of particles with phase space coordinates $(\boldsymbol{r}, \boldsymbol{v})$, which can be projected on the sky, giving (α_m, δ_m) and a radial velocity v_m. For each particle, we also have the probability $p_\star$ of tagging a star. Denoting by r the projected distance of a particle to it's closest neighbour, then $p_\star/r^2$ can be used as a measure for the surface brightness Σ. For each line of sight (LOS) to a star at position (α_d, δ_d), we select all particles in the N-body models along that LOS. We then fit independent Gaussian functions to all v_m, Σ_m along the LOS, i.e. we assume that v_m and Σ_m are uncorrelated. The product of these Gaussians then reads

$$\varphi\left(v, \Sigma|\bar{v}_m, \bar{\Sigma}_m, \sigma_{v_m}, \sigma_{\Sigma_m}\right) = \frac{1}{2\pi\sigma_{v_m}\sigma_{\Sigma_m}} \exp\left(-\frac{1}{2}\left[\frac{(v-\bar{v}_m)^2}{\sigma^2_{v_m}} + \frac{(\Sigma-\bar{\Sigma}_m)^2}{\sigma^2_{\Sigma_m}}\right]\right) . \tag{21}$$

We convolve this intrinsic distribution of our N-body model with Gaussian measurement errors, centred on the simulated value,

$$\varphi\left(v_d, \Sigma_d|v, \Sigma, \sigma_{v_d}, \sigma_{\Sigma_d}\right) , \tag{22}$$

where we assumed that the errors on v_r and Σ are uncorrelated. The convolution as a function of (v_d, Σ_d) then reads

$$\varphi^*\left(v_d, \Sigma_d\right) = \iint\limits_{\{v,\Sigma\}} \varphi\left(v_d, \Sigma_d|v, \Sigma, \sigma_{v_d}, \sigma_{\Sigma_d}\right) \varphi\left(v, \Sigma|\bar{v}_m, \bar{\Sigma}_m, \sigma_{v_m}, \sigma_{\Sigma_m}\right) dv\, d\Sigma \tag{23}$$

$$= \varphi\left(v_d, \Sigma_d|\bar{v}_m, \bar{\Sigma}_m, \sqrt{\sigma^2_{v_d} + \sigma^2_{v_m}}, \sqrt{\sigma^2_{\Sigma_d} + \sigma^2_{\Sigma_m}}\right) . \tag{24}$$

This convolution is schematically shown in figure 10.

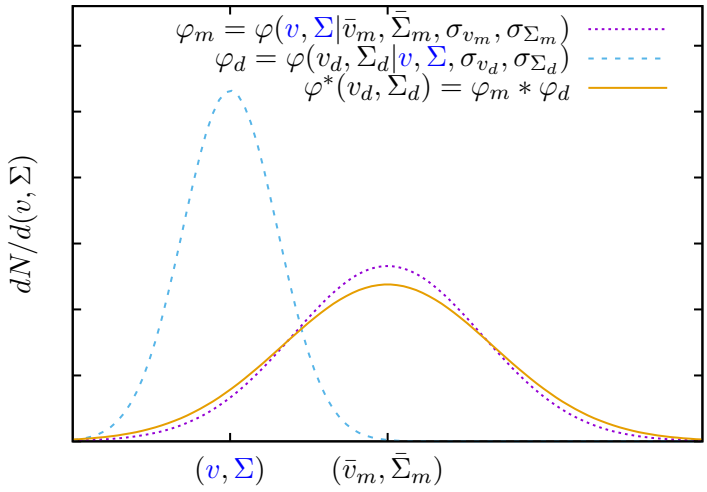

Figure 10: Convolution of the model distribution φ_m with Gaussian measurement errors φ_d.

Then the product of φ^* computed for all observational data points is our likelihood $P(d|\theta_\alpha)$:

$$P(d|\theta_\alpha) = \prod_{\{v_d, \Sigma_d\}} \varphi^*\left(v_d, \Sigma_d\right) \ . \tag{25}$$

We use flat priors in $R, a, r_\star, \lg(M)$ and two delta function priors for γ. Our constraint on the central slope γ then becomes

$$P(\gamma = 1|d) = \sum_{\alpha|\gamma=1} \frac{P(d|\theta_\alpha)P(\theta_\alpha)}{P(d)} \tag{26}$$

where $P(\theta_\alpha)$ is the flat prior and

$$P(d) = \sum_\alpha P(d|\theta_\alpha)P(\theta_\alpha) \tag{27}$$

is the normalization.

Figures 11 to 13 show mock measurements of surface brightness Σ, radial velocity v and projected velocity dispersion $\sigma_\parallel$ for a cored dSph model with $5 \times 10^{10}\,\mathrm{M}_\odot$, $a = 4\,\mathrm{kpc}$, $r_\star/a = 0.2$ on an orbit with $R_{\mathrm{apo}} = 70\,\mathrm{kpc}$. The lines of sight are taken for the dataset of Peñarrubia et al. (2011) on which we also base our preliminary analysis. This dataset does, due to bad weather, not contain any measurements for the centre of Sgr.

The data is smoothed over areas containing 1 per cent of the Sgr luminosity to achieve good statistics regarding the stellar tracers, evidently at the cost of angular resolution. Grey circles around each LOS indicate the area over which the data is averaged. In the central regions, $r_{\mathrm{smooth}} \approx 0.3°$, while r_{smooth} grows in the outer, fainter regions to the order of unity. For cuspy progenitors, because of the higher number of DM particles, the smoothing area can be chosen smaller.

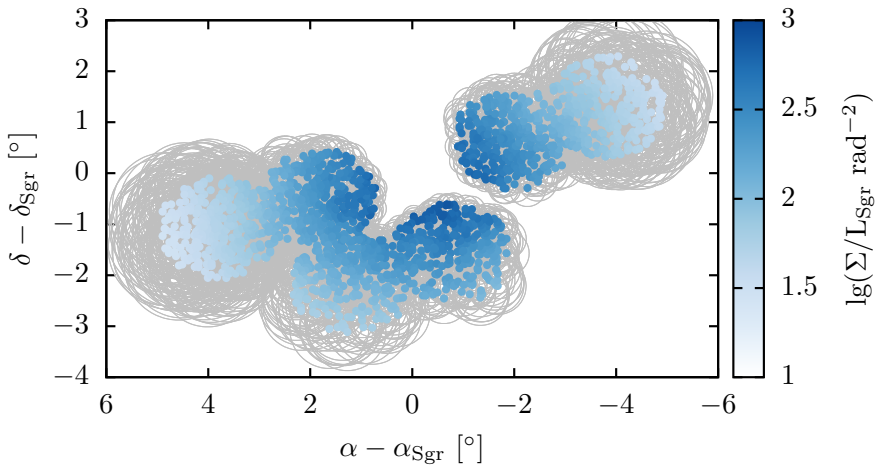

Figure 11: Surface brightness Σ samples for a cored dSph model with $5 \times 10^{10}\,\mathrm{M}_\odot$, $a = 4\,\mathrm{kpc}$, $r_\star/a = 0.2$, $R_{\mathrm{apo}} = 70\,\mathrm{kpc}$. LOS match the Peñarrubia et al. (2011) dataset.

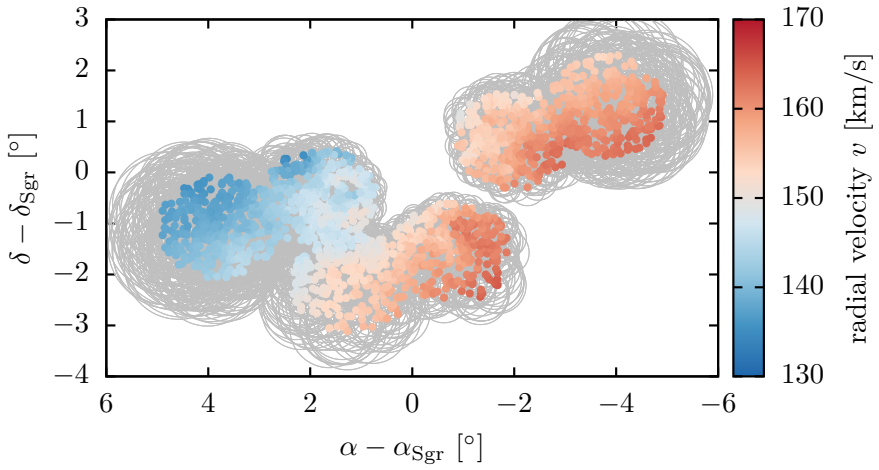

Figure 12: Radial velocity v samples for the cored dSph model of fig. 11.

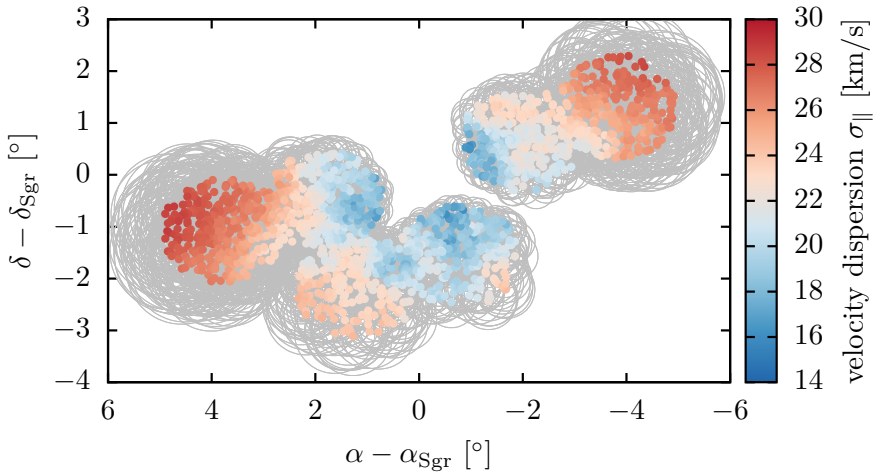

Figure 13: Velocity dispersion v samples for the cored dSph model of fig. 11.

3.2 Isotropic systems in equilibrium

For the special case of models in dynamical equilibrium, the velocity dispersion for a Plummer sphere of stellar tracers embedded in a Dehnen DM halo can be obtained analytically from the Jeans equation. We use this to test the statistical distributions determining the Likelihood $P(d|\theta_\alpha)$ against analytical predictions. For isotropic systems, from equation 14 (page 12) but with a systemic mean square velocity $\langle v\rangle^2 > 0$ we have

$$\langle v^2(r)\rangle - \langle v\rangle^2 = \frac{1}{\nu}\int_r^\infty dr\ \nu\frac{d\Phi}{dr} \qquad \text{where} \qquad \nu = \varrho_\star/m_\star\ . \tag{28}$$

We center this equilibrium model at the phase space coordinates $(\boldsymbol{r},\boldsymbol{v})_{\rm Sgr}$ corresponding to the centre of the Sagittarius dwarf galaxy, assuming for $\boldsymbol{v}$ the usual constraints with $R_{\rm apo} = 75\,{\rm kpc}$. We then project the model on the sky and compute the observables projected along the line of sight. Following the notation of Binney & Tremaine (2008, chap. 4.8.1), the projected density of stellar tracers becomes

$$\nu_\parallel = \int_0^\infty \nu(r)dx_\parallel \qquad \text{where} \qquad r = |\boldsymbol{x}_\parallel - \boldsymbol{x}_{\rm Sgr}|\ , \tag{29}$$

and the projected mean square velocity follows as

$$\langle v^2(r)\rangle_\parallel = \frac{1}{\nu_\parallel}\int_0^\infty \nu(r)\langle v^2(r)\rangle dx_\parallel\ . \tag{30}$$

The projected systemic velocity is just the inner product of the systemic velocity $\boldsymbol{v}$ with a unit vector $\hat{\boldsymbol{x}}_\parallel$ pointing along the line of sight: $\langle v\rangle_\parallel = \hat{\boldsymbol{x}}_\parallel \cdot \boldsymbol{v}$.

Figure 14 shows the difference between the map of projected velocities for the analytical closed-form model and the corresponding N-body model for a low-mass ($10^{10}\,{\rm M}_\odot$) cored progenitor with deeply segregated stellar component ($r_\star/a = 0.2$) in an extended DM halo ($a = 5\,{\rm kpc}$). As for the specific (critical) model in fig. 14 the number of particles which trace the stellar component is particularly low ($M(r_\star)/M = r_\star^3/(r_\star + a)^3 \approx 0.5$ per cent), the uncertainty in velocity rises up to $5\,{\rm km/s}$.

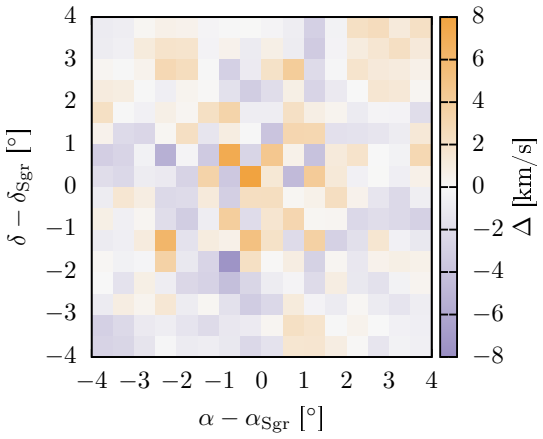

Figure 14: Difference between projected velocities for the isotropic equilibrium model and the corresponding N-body model ($M = 10^{10}\,{\rm M}_\odot$, $a = 5\,{\rm kpc}$, $r_\star/a = 0.2$).

4 The model catalogue

We did run simulations for 3600 different initial conditions with spacing of 1 kpc in DM scale radius a, $10^10\,\mathrm{M}_\odot$ in total mass M and 2 kpc in apocentre distance R_apo for cuspy and cored progenitors, that is, in total 7200 different sets of initial conditions. Of these 7200 sets, 4 per cent disrupted or did not produce models within the observational constraints. Walking diagonally through parameter space, this excluded another 57 per cent of data sets. The remaining 39 per cent of initial conditions are those we will analyse in the following. Note that only 10 per cent of the necessary computation time was spent on disrupting models. Table 3 below lists the exact numbers.

Table 3: Overview of the number of simulation runs.

initial conditions	7200
executed simulations	3099
models within the constraints	2783
not reproducing the constraints / disrupted	316

4.1 Disruption of cored progenitors

Cored progenitors can disrupt during the tidal interaction with the host halo, while we did not obtain any disrupting cuspy models. Figure 15 shows for each total mass M the cored, non-disrupting model with lowest initial density in parameter space for different values of R_apo. It

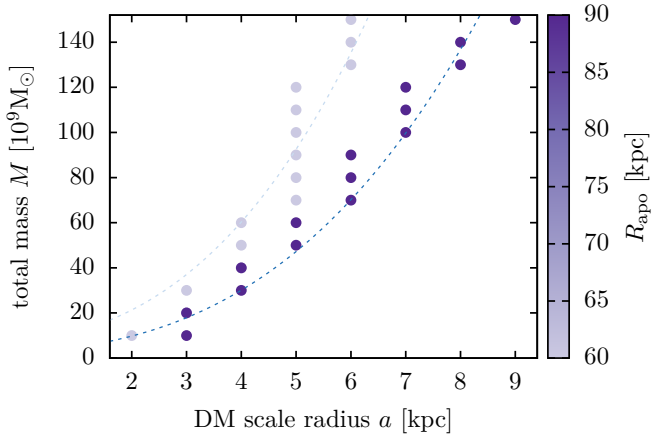

Figure 15: *Lines of disruption* for cored models. For each total mass M, the model with lowest initial density is shown in parameter space. The dashed curves are fits made assuming $M(r_t)/r_t^3$ =const.

is clear from figure 15 that for a fixed DM scale radius a, higher mass models and those with larger apocentre distances disrupt less easily. This can be approximately reproduced analytically imposing the condition that

$$M(<r_t)/r_t^3 \approx \mathrm{const} \quad \text{for } t=0 \qquad \text{(approximative criterion for survival)}\ . \tag{31}$$

Remembering that for Dehnen profiles

$$M(<r) = M\left(\frac{r}{(r+a)}\right)^{3-\gamma} , \tag{32}$$

we get for the approximative criterion for cored galaxies ($\gamma = 0$):

$$\frac{M(<r_t)}{r_t^3} = \frac{M}{(r+a)^3} \approx \text{const} . \tag{33}$$

For Keplerian orbits with numerical eccentricity $e = (r_a - r_p)/(r_a + r_p)$ and cored, split power-law potentials, analytical expressions for r_t do exists (see Read et al., 2006, section 2.3). But already from classical and much more intuitive King formula

$$r_t \approx r_p \left(\frac{M_{\rm sat}}{M_{\rm host}(3+e)}\right)^{1/3} \tag{34}$$

some hindsight can be obtained by overcoming the limits of the point-mass approximation underlying this formula using for the satellite mass $M_{\rm sat} = M(<r_t)$. Inserting the above equation for r_t in equation 33 yields a third-order polynomial for $M(a)$ with just one free parameter, which is fitted by the dashed curves shown in figure 15.

4.2 Orbital decay

To generate initial conditions, we integrate point-mass orbits backwards in time using a simple Runge Kutta scheme of $4^{\rm th}$ order, starting from the current position of Sgr in phase space. We obtain periodic galactocentric distances of Sgr in function of time as shown in figure 16. For massive, low-density progenitors however, simulated orbits starting from the initial conditions generated using the point-mass approximation have decaying apocentre distances $R_{\rm apo}$. Figure 17 shows the orbit of a cuspy progenitor with $M = 5 \times 10^{10}\,{\rm M}_\odot$, $a = 4\,{\rm kpc}$ (in projection on the Sgr orbital plane), while figure 18 shows the decaying galactocentric distance over time for the same progenitor.

Let me point out that our N-body code does not include (Chandrasekhar-) dynamical friction. The orbital decay must therefore be a consequence of the tidal interaction. To better understand

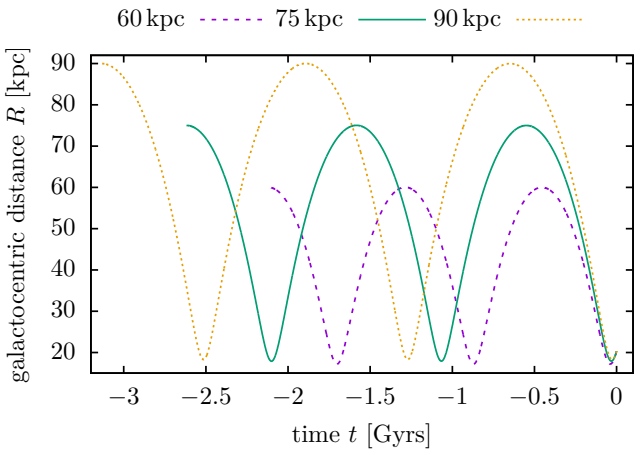

Figure 16: Point-mass orbit approximations for Sgr, integrated backwards in time for 3 orbital periods in an analytical axis-symmetric host halo.

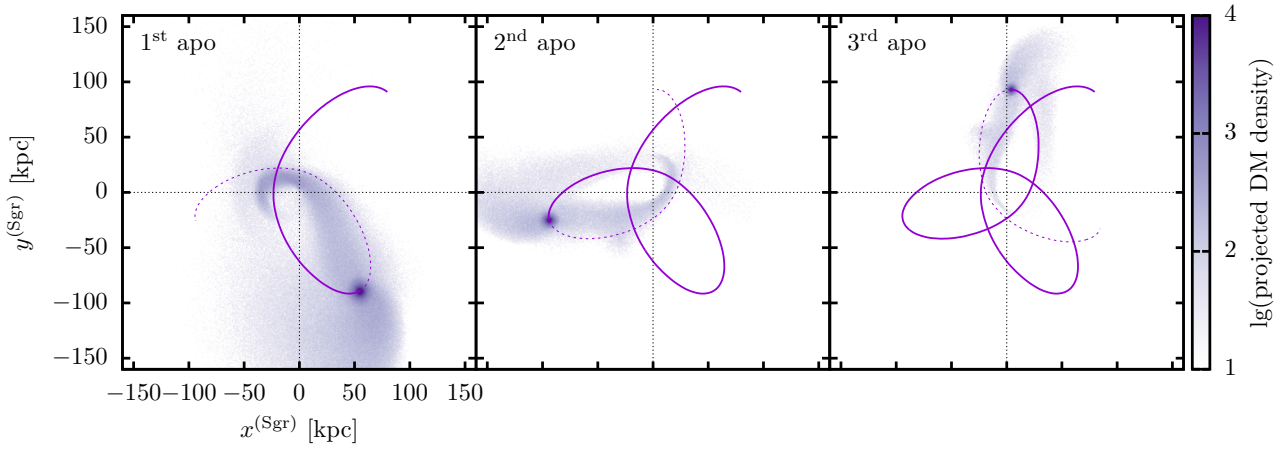

Figure 17: Orbit of a progenitor with $M = 5\times10^{10}\,\mathrm{M}_\odot$, $a = 4\,\mathrm{kpc}$. Only the tidal debris stripped at the most recent pericentric passage is shown in correspondence to figure 19.

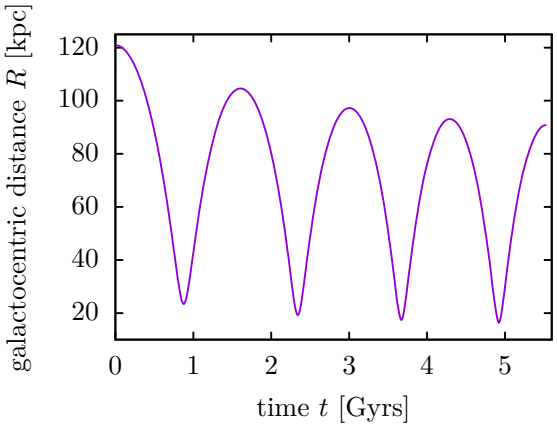

Figure 18: Decaying apocentre distance R_{apo} for a cuspy progenitor with $M = 5 \times 10^{10}\,\mathrm{M}_\odot$, $a = 4\,\mathrm{kpc}$.

this effect, we study how the distribution of single-particle energies dN/dE as measured in the host frame evolves during tidal stripping. At every pericentric passage, the orbital energy of the progenitor is re-distributed between the bound particles making up the remnant progenitor and the unbound particles escaping through the Lagrangian points, forming the leading and trailing tidal streams. Figure 19 shows this energy re-distribution for the progenitor of figure 17, measured at three different snapshots taken at apocentre. Only particles stripped at the pericentric passage preceding the snapshot are used to compute dN/dE. We see that the average energy of the bound particles decreases, as expected from the decaying apocentre distance. The particles stripped at the preceding pericentric passage forming leading and trailing stream are not equal in number, as can be deduced from the areas below the red dashed curves of figure 19, showing dN/dE for stream particles. A larger fraction of particles is escaping through L_2, forming the energetically higher (i.e. less bound to the host) trailing stream. For massive progenitors – for which the effect is largest – the Lagrangian points lie at a larger distance to the progenitor centre. As a consequence, the potential can't be assumed to behave linearly on

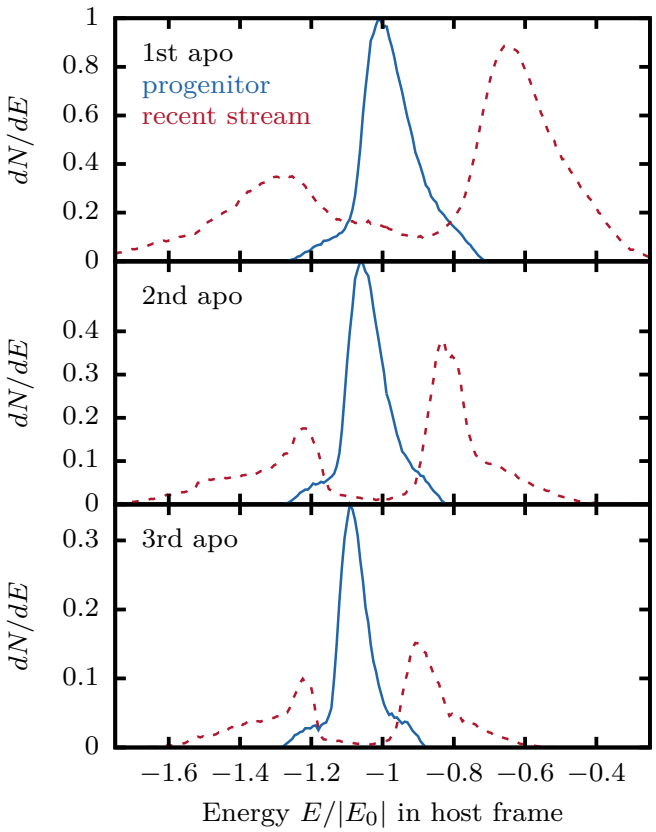

Figure 19: Energy as measured in the host frame for particles which are bound (blue) or unbound (red) to the progenitor (cuspy dSph with $M = 5 \times 10^{10}\,\mathrm{M}_\odot$, $a = 4\,\mathrm{kpc}$, see figure 17 for orbit). Snapshots are taken at the 1st, 2nd and 3rd apocentre. For the unbound particles forming the tidal stream, only the particles stripped at the pericentric passage preceding the snapshot are taken into account.

that scale, and even for streams balanced in number of particles the orbital energy lost to the trailing stream does not balance the energy gained from the more tightly bound leading stream. We compensate for this tidal orbital decay when generating initial conditions using the iterative procedure in energy E, angular momentum $\hat{\boldsymbol{L}}$ and orbital phase φ as described in section 2 (see e.g. equation 19 for E).

4.3 Analysis and discussion of selected models

In the following, we list a set of selected cuspy and cored N-body models for the Sgr galaxy. We show both the projection of the models in celestial coordinates (α, δ) as well as detailed maps of the central 10° for surface brightness Σ, radial velocity v and projected velocity dispersion $\sigma_\parallel$. While the dynamics of the models is governed by the underlying DM, we plot only observable quantities as calculated from the stellar tracers for different segregations $r_\star/a$. We only show models with DM scale radii which did not disrupt. We also limit this selection to models with $R_\mathrm{apo} = 70\,\mathrm{kpc}$ to highlight observable differences in morphology and kinematics due to structural differences rather than orbital ones.

Model 1: $M = 2 \times 10^{10}\,\mathrm{M}_\odot$, $a = 3\,\mathrm{kpc}$, $r_\star/a = 0.2$, $R_\mathrm{apo} = 70\,\mathrm{kpc}$

(1.0) core:

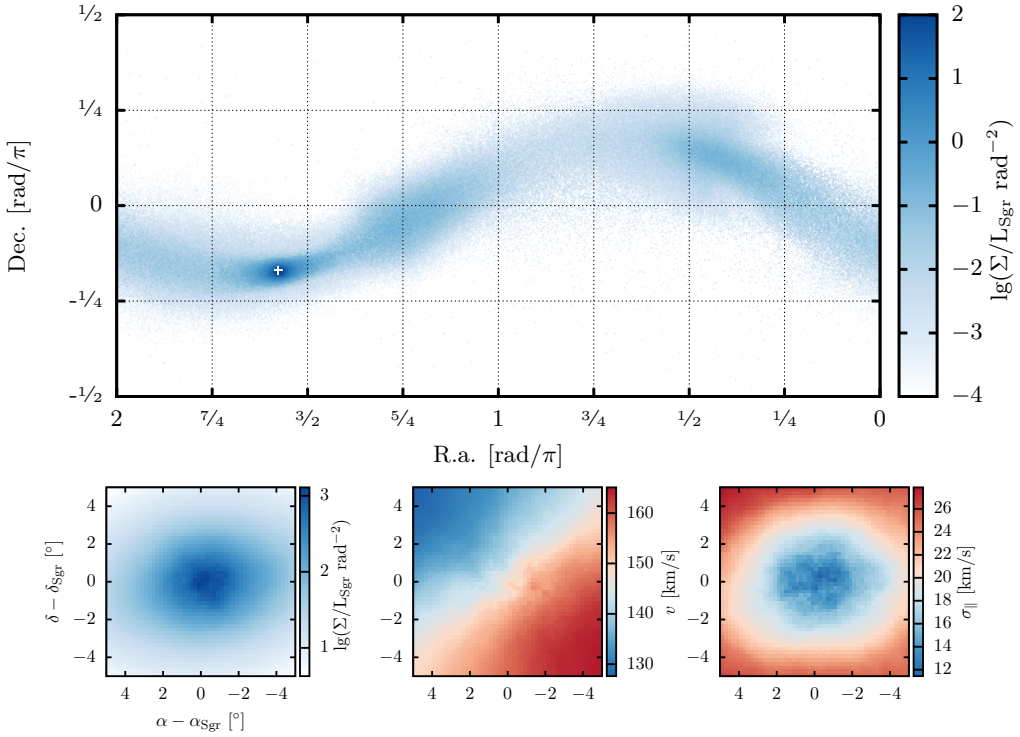

(1.1) cusp:

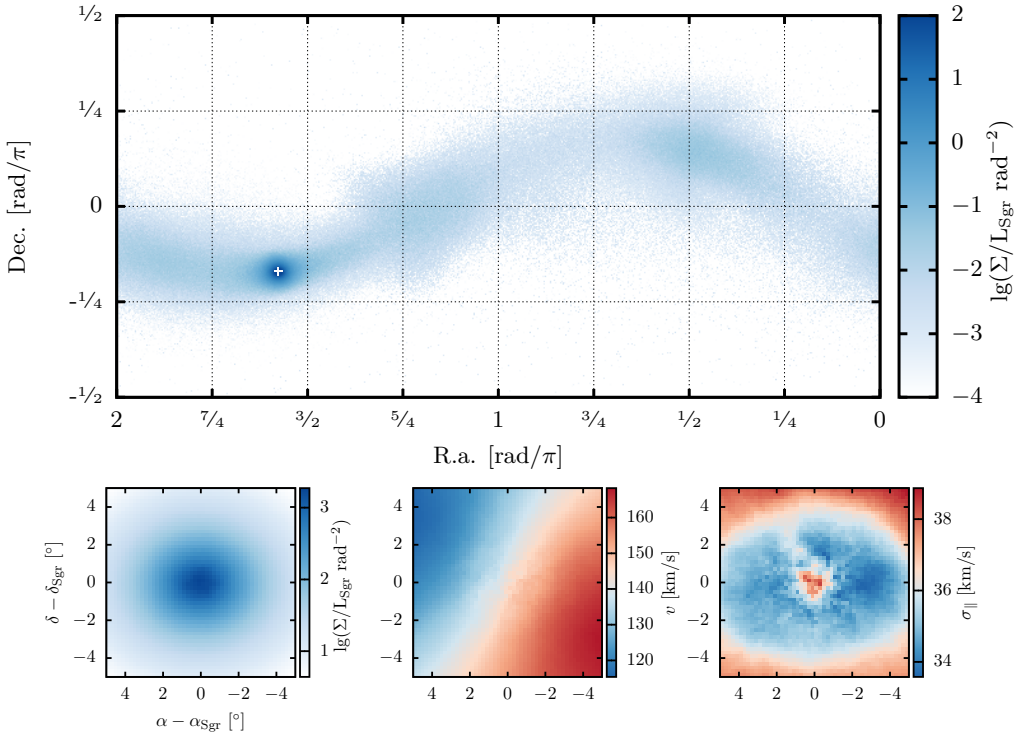

Model 2: $M = 5 \times 10^{10}\,\mathrm{M}_\odot$, $a = 4\,\mathrm{kpc}$, $r_\star/a = 0.2$, $R_\mathrm{apo} = 70\,\mathrm{kpc}$

(2.0) core:

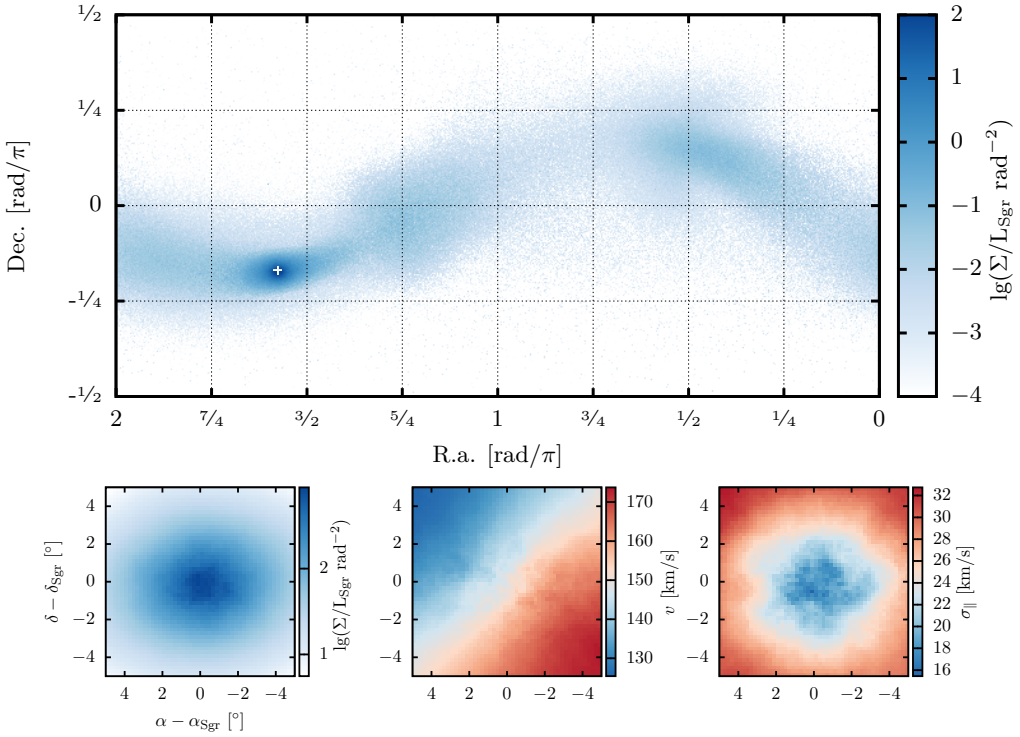

(2.1) cusp:

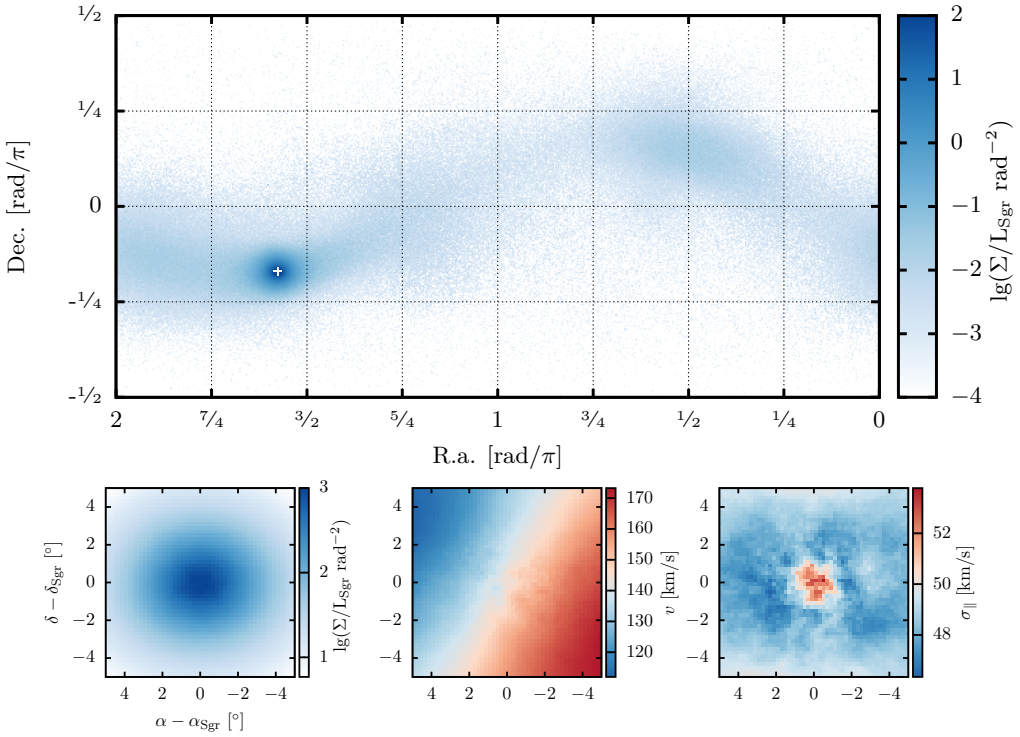

Model 3: $M = 5 \times 10^{10}\,\mathrm{M}_\odot$, $a = 4\,\mathrm{kpc}$, $r_\star/a = 0.6$, $R_\mathrm{apo} = 70\,\mathrm{kpc}$

(3.0) core:

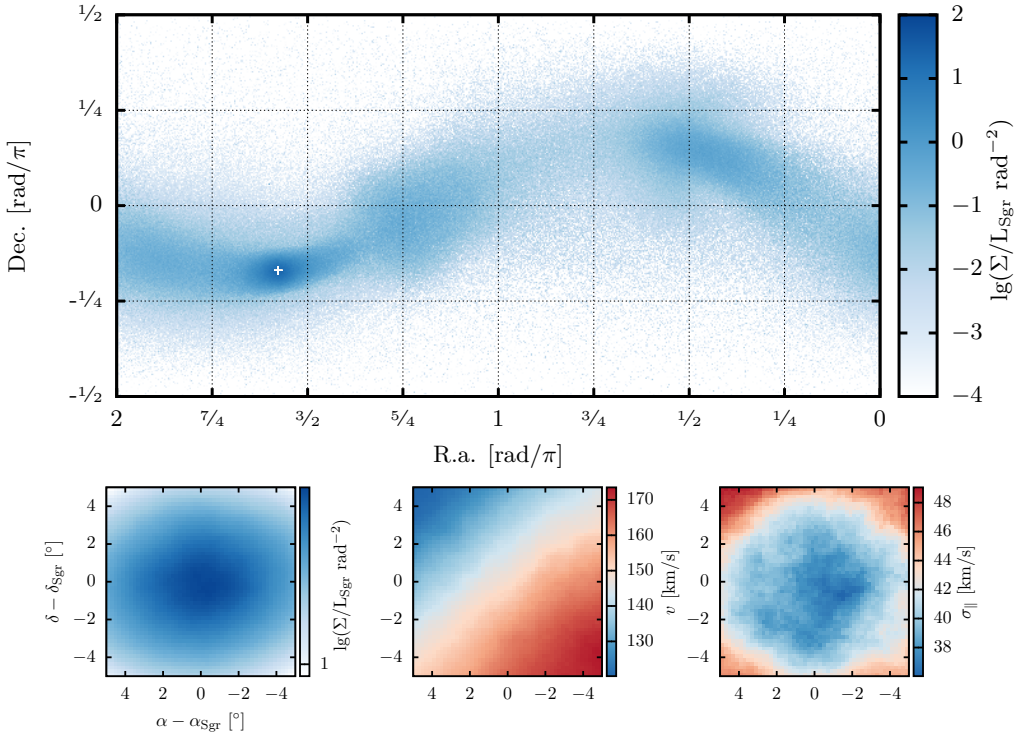

(3.1) cusp:

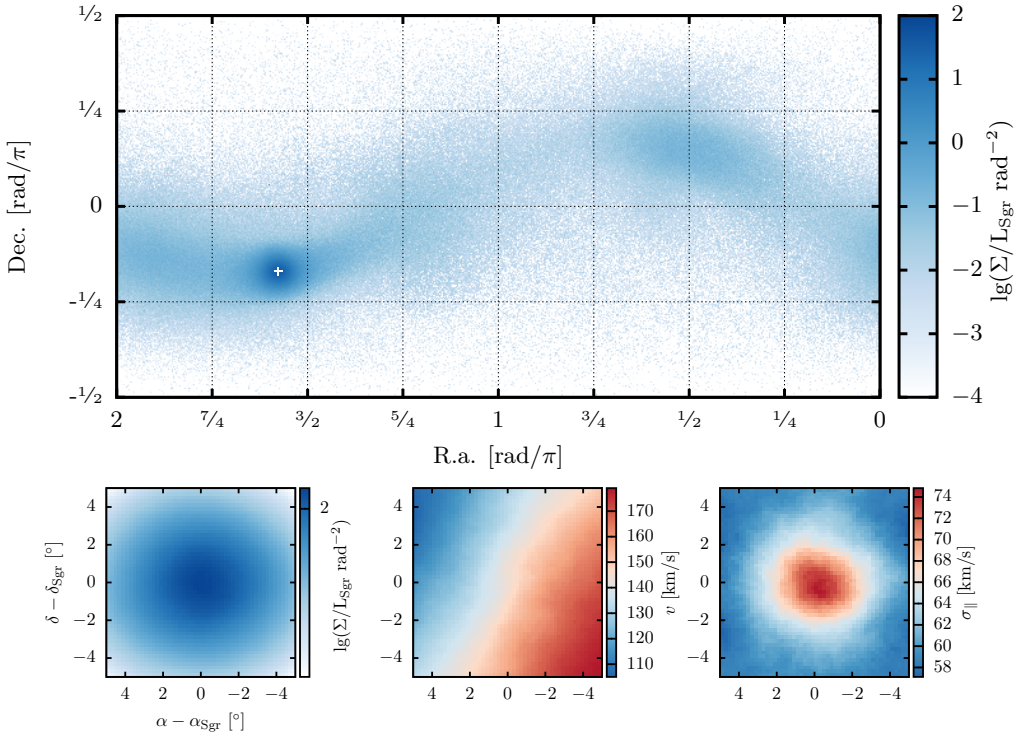

Model 4: $M = 10^{11}\,\mathrm{M}_\odot$, $a = 4\,\mathrm{kpc}$, $r_\star/a = 0.2$, $R_\mathrm{apo} = 70\,\mathrm{kpc}$

(4.0) core:

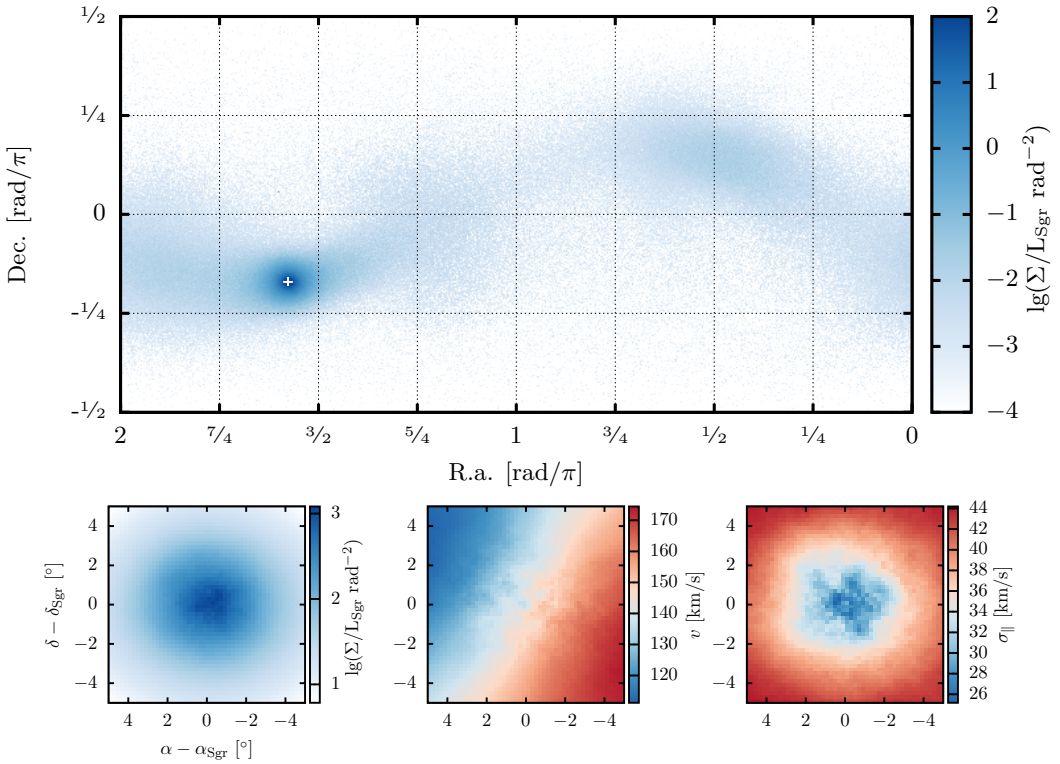

(4.1) cusp:

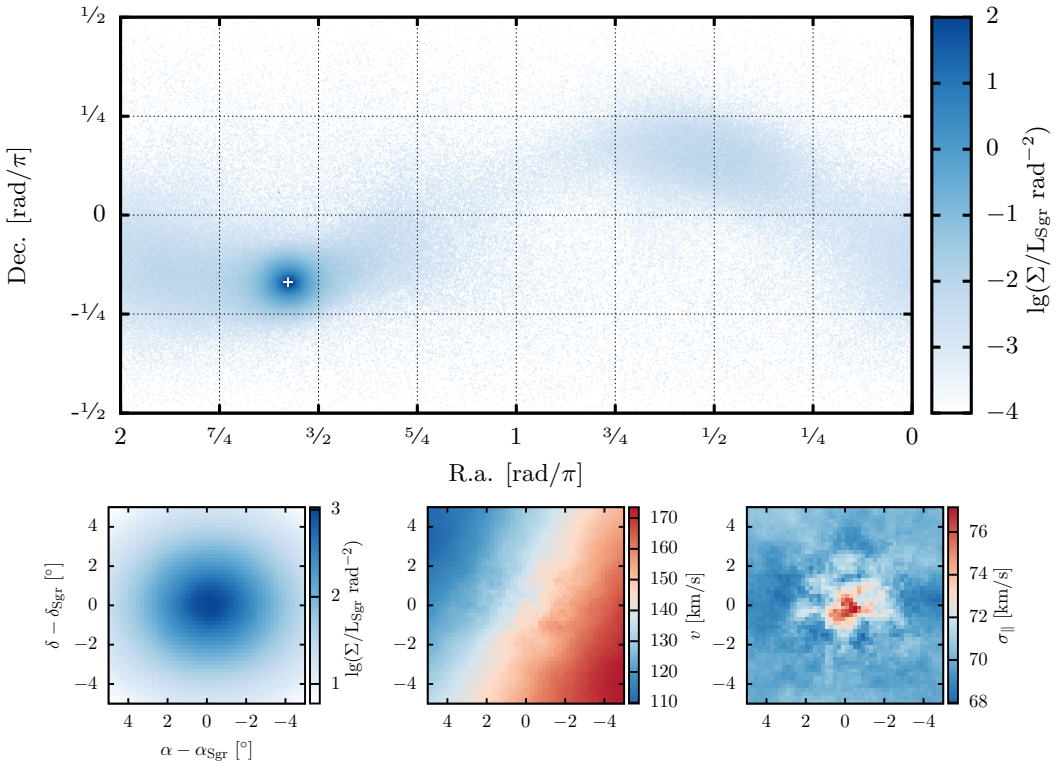

Discussion of selected models

The range in parameter space of the simulated Sagittarius models is large and leads to morphologically and kinematically different remnant progenitors and associated tidal streams. Selected models listed in this chapter are shown in groups of equal initial mass M, scale radius a, stellar segregation $r_\star/a$ and most recent apocentre distance $R_{\rm apo}$. They do differ regarding the central slope γ of the DM profile (cusp/core), and as the tidal orbital decay depends on the distribution of DM within the dwarf galaxy, their orbits differ slightly.

Comparing cuspy and cored models with equal initial physical properties, we see that cored models are more perturbed by tidal forces than their cuspy counterparts: the density profiles are elongated in the direction of orbital motion (compare left panels in second row for each of the models). The projected line-of-sight velocity shows a gradient inclined by different angles with respect to the chosen celestial coordinate system, as for perturbed models a non-zero velocity in the rest frame of the dwarf galaxy is added to the orbital motion compare central panels in second row for each of the models). Note that for models with projected velocity dispersion $\sigma_\parallel$ increasing towards the centre, the noise in the maps of the line-of-sight velocity increases towards the centre, as is to be expected for models with a finite number of particles. The sign of the projected radial velocity dispersion gradient is different for cuspy and cored models, as is the size of the plateau with near-constant velocity dispersion: e.g. the cored model 3.0 with $r_\star/a = 0.6$ has, within the field of view of $\pm 5°$, a constant projected velocity dispersion of $(38 \pm 1)\,\mathrm{km/s}$.

The associated stellar tidal streams as projected on the celestial sphere are shown in the top panels for each of the listed model. We did not try to match the observed position of the Sagittarius stream on the sky, which is very sensitive to the choice of the host potential (see e.g. Law et al., 2005; Peñarrubia et al., 2011), as we are mainly interested in the kinematic properties of the progenitor in this work. From models 2 and 3, which have equal DM properties, we see that streams of progenitors with larger segregation parameter $r_\star/a$ are brighter than streams with smaller values of $r_\star/a$.

The cuspy models from the simulated interval of masses and scale radii do not lose sufficient quantities of mass during the past tidal evolution to reach velocity dispersions in the order of 11 km/s as observed for the Sagittarius dwarf galaxy (see e.g. Ibata et al., 1997). We will therefore run additional simulations for lower-mass cuspy progenitors. For models with low surface brightness outside of the Sagittarius centre – for example cuspy models which lost only small quantities of their total mass and did therefore only form faint streams, or cored models with small segregation parameter $r_\star/a$ – Poisson noise, especially for second-order quantities like the projected velocity dispersion $\sigma_\parallel$, becomes problematic: larger smoothing regions have to be chosen to obtain physical sensible estimates for the stellar observables, at the expense of angular resolution.

5 Summary and future work

We have studied the tidal evolution of dSph galaxies and their associated tidal streams in static, axis-symmetric host haloes using high-resolution N-body simulations. The disparate evolution of cuspy and cored progenitors drives observable differences in kinematics and morphology of the associated stellar tidal streams: streams of cored dSphs are, normalizing the stream properties by the corresponding progenitor properties, hotter and narrower than streams of cuspy models. We have shown that combined measurement of properties of both a tidal stream and its remnant progenitor puts strong constraints on the distribution of DM within the progenitor. While the application of this method is straightforward for dSph galaxies in dynamical equilibrium, where the galaxies evolve along well-defined *tidal tracks* independently of orbit or scale, for dSph galaxies perturbed by tidal forces – like the Sagittarius dwarf galaxy – a slightly different approach has to be followed to generate suitable initial conditions for modelling the tidal evolution.
For this purpose, we developed a catalogue of non-equilibrium N-body models of the Sagittarius dwarf galaxy and its tidal stream. Each model consists of 10^6 DM particles. The stellar component is modelled by associating mass-to-light ratios to the individual DM particles. An iterative procedure is used to match initial conditions to the current constraints on the orbit of the Sagittarius dwarf, compensating also for the tidally-induced orbital decay. To compare the N-body models to observational data, we developed a Bayesian statistical model which allows us to constrain the probabilities of the model parameters.

We will run additional simulations for lower-mass cuspy progenitors to match the observed central velocity dispersion of Sgr.
Using radial velocity measurements for stars in the Sgr dwarf galaxy obtained from the Anglo-Australian Telescope (AAT), we will apply the Bayesian statistical model described in this work to the catalogue of N-body models developed during this project. The new AAT data also covers the centre of Sgr, missing in the 2011 dataset to which we had access to so far. We have access to Gaia-ESO survey data, which we will use to determine the properties of the stellar tidal stream of Sgr, necessary to constrain the distribution of DM within Sgr.
It is still to be understood in detail how the choice of the host potential $\Phi_{\rm MW}$ reflects upon the relative observable differences between cuspy and cored models. Changes to the host potential $\Phi_{\rm MW}$ are necessary if one wishes to match the position of the Sgr stream as projected to the celestial sphere to observational data. This also leaves the question of the observed bifurcation in the Sgr stream unanswered. Also the possibly different effect of a time-evolving host halo on cored and cuspy models has to be taken into consideration.
So far, our analysis is focused on finding observable differences between density profiles with either a central slope of $d\ln\rho/dr = -\gamma = -1$ (cusp) or $d\ln\rho/dr = 0$ (core). The excludes the possibility in parameter space of less steep central slopes $0 < \gamma < 1$ e $r_\star/a$. It is yet to be tested how well the DM profile can be constrained by the models developed so far, and if (non-binary) predictions on the value γ are feasible.

Acknowledgements

Over the last years, the study of gravitating systems became a highly fascinating and enjoyable part of my life, and I would like to use the opportunity to thank my teachers Jorge Peñarrubia and Giuseppe Tormen for their amazing guidance. The frequent and vivid discussions were not only substantial to resolve problems along the way, but also helped me to develop a better understanding of the physical processes which formed the universe around us.

In her function as co-examiner, I would like to thank Michela Mapelli for her detailed and helpful comments both on the thesis text as well as on the presentation.

I also want to thank Jorge Penãrrubia for the year of collaboration on this project at the University of Edinburgh, as well as for the computation time at the IAA in Granada and the challenging and motivating opportunity to present the project at different international conferences. I am excited about the dynamical and cosmological adventures awaiting me during my following PhD studies under his supervision.

Finally I want to thank Giuseppe Tormen for his enthusiastic support over the last two and a half years which undoubtedly deepened my fascination for cosmology and fundamental physics. I also want to thank him for the detailed feedback on the thesis presentation, for the computation time at the Department of Physics and Astronomy in Padova and for the quiet office space I had access to when working on this project.

References

Amorisco N. C., 2015, MNRAS, 450, 575

Amorisco N. C., Evans N. W., 2012, MNRAS, 419, 184

Belokurov V., et al., 2014, MNRAS, 437, 116

Binney J., Tremaine S., 2008, Galactic Dynamics: Second Edition. Princeton University Press

Breddels M. A., Helmi A., 2013, A&A, 558, A35

Bullock J. S., Johnston K. V., 2005, ApJ, 635, 931

Dehnen W., 1993, MNRAS, 265, 250

Di Cintio A., Brook C. B., Macciò A. V., Stinson G. S., Knebe A., Dutton A. A., Wadsley J., 2014, MNRAS, 437, 415

Dinescu D. I., Girard T. M., van Altena W. F., López C. E., 2005, ApJ, 618, L25

Errani R., Peñarrubia J., Tormen G., 2015, MNRAS, 449, L46

Fellhauer M., Kroupa P., Baumgardt H., Bien R., Boily C. M., Spurzem R., Wassmer N., 2000, NA, 5, 305

Hernquist L., 1990, ApJ, 356, 359

Ibata R. A., Wyse R. F. G., Gilmore G., Irwin M. J., Suntzeff N. B., 1997, AJ, 113, 634

Law D. R., Johnston K. V., Majewski S. R., 2005, ApJ, 619, 807

Lovell M. R., Frenk C. S., Eke V. R., Jenkins A., Gao L., Theuns T., 2014, MNRAS, 439, 300

Ludlow A. D., Navarro J. F., Angulo R. E., Boylan-Kolchin M., Springel V., Frenk C., White S. D. M., 2014, MNRAS, 441, 378

Macciò A. V., Paduroiu S., Anderhalden D., Schneider A., Moore B., 2012, MNRAS, 424, 1105

Majewski S. R., Skrutskie M. F., Weinberg M. D., Ostheimer J. C., 2003, ApJ, 599, 1082

Massari D., Bellini A., Ferraro F. R., van der Marel R. P., Anderson J., Dalessandro E., Lanzoni B., 2013, ApJ, 779, 81

Miyamoto M., Nagai R., 1975, PASJ, 27, 533

Moster B. P., Naab T., White S. D. M., 2013, MNRAS, 428, 3121

Navarro J. F., Eke V. R., Frenk C. S., 1996, MNRAS, 283, L72

Navarro J. F., Frenk C. S., White S. D. M., 1997, ApJ, 490, 493

Niederste-Ostholt M., Belokurov V., Evans N. W., Peñarrubia J., 2010, ApJ, 712, 516

Nipoti C., Binney J., 2015, MNRAS, 446, 1820

Peñarrubia J., Navarro J. F., McConnachie A. W., 2008, ApJ, 673, 226

Peñarrubia J., et al., 2011, ApJ, 727, L2

Peñarrubia J., Pontzen A., Walker M. G., Koposov S. E., 2012, ApJ, 759, L42

Pontzen A., Governato F., 2014, Nature, 506, 171

Pryor C., Piatek S., Olszewski E. W., 2010, AJ, 139, 839

Read J. I., Wilkinson M. I., Evans N. W., Gilmore G., Kleyna J. T., 2006, MNRAS, 366, 429

Richardson T., Fairbairn M., 2014, MNRAS, 441, 1584

Rocha M., Peter A. H. G., Bullock J. S., Kaplinghat M., Garrison-Kimmel S., Oñorbe J., Moustakas L. A., 2013, MNRAS, 430, 81

Siegel M. H., et al., 2007, ApJ, 667, L57

Strigari L. E., Frenk C. S., White S. D. M., 2014, preprint, (arXiv:1406.6079)

Vogelsberger M., Zavala J., Simpson C., Jenkins A., 2014, MNRAS, 444, 3684

Walker M. G., Peñarrubia J., 2011, ApJ, 742, 20